ELSEVIER

Turbulence statistics in the stagnation region of an axisymmetric impinging jet flow

Koichi Nishino, Masanori Samada, Keiichi Kasuya, and Kahoru Torii
Department of Mechanical Engineering and Materials Science, Yokohama National University, Yokohama, Japan

Turbulence statistics in the stagnation region of an axisymmetric jet impinging vertically on a flat plate are reported. The measurements were made in a submerged water jet facility at a Reynolds number of approximately 13,000 based on the nozzle exit velocity and the nozzle diameter. Particle-tracking velocimetry was used for the measurement of highly turbulent flows near the stagnation point. The axial mean momentum balance was examined to clarify the effect of the turbulent normal stress on the axial mean momentum transport. It was found that the turbulent normal stress of the axial component made a substantial contribution to the increase in the static pressure near the impingement wall. Detailed distributions of the turbulent stresses and the triple correlations of velocity fluctuations are presented. The state of turbulence was studied by means of an invariant map of the turbulent stress anisotropy. It was revealed that the turbulence was close to an axisymmetric state in the stagnation region. The budget equation for the turbulent kinetic energy evaluated from the present data shows that the net negative production takes place in the vicinity of the wall. This negative production is compensated by the pressure diffusion. Other unique features of the budget for the turbulent kinetic energy are also discussed.

Keywords: turbulent flow, axisymmetric impinging jet flow, stagnation region, turbulence statistics, turbulent kinetic energy, particle-tracking velocimetry

Introduction

An axisymmetric jet flow impinging vertically on a flat plate is the flow used in many industrial applications. This is because the impingement can enhance heat and mass transfer rates in the stagnation area of an impingement surface. The multijet cooling of arrays of electronic packages, the impingement cooling of the inner surfaces of turbine blade, and the impingement drying of textile, paper, and film are typical applications. The impinging flow is also important from a turbulence modeling point of view. This is because the existing turbulence models are mostly tested against flows parallel to the wall; hence, they may not be able to give satisfactory predictions for the impinging flows whose streamlines are basically not parallel to the wall. In fact, some recent numerical calculations (e.g., Kato and Launder 1993; Craft et al. 1993) have revealed several problems in the existing turbulence models; i.e., the standard k-ε model tends to overestimate the turbulent kinetic energy in the stagnation region, while the wall-reflection term in the stress equation model proposed by Gibson and Launder (1978) has an undesired effect on the turbulence redistribution mechanism near the impingement surface. Although much effort has been directed toward improving such shortcomings in existing turbulence models, the progress has been hindered somewhat by the lack of detailed experimental data, particularly in the stagnation region.

An early measurement of a circular impinging jet flow was made by Donaldson et al. (1971). They presented centerline behaviors of the axial mean velocity and turbulence intensities of both axial and radial components. Beltaos and Rajaratnam (1974), Era and Saima (1975), and Ennohji and Asanuma (1982) performed measurements of velocity fields by using hot-wire anemometry. They analyzed the velocity data with a view to finding out similarity laws for the mean velocity profile and the wall pressure distribution. In recent years, more detailed measurements of turbulence quantities in the stagnation region were carried out by Sudou and Hibara (1991), Barata et al. (1993), and Cooper et al. (1993). Sudou and Hibara used a rotating probe with a slant hot wire to obtain statistical properties of all three velocity components. They presented contour maps of the Reynolds stresses and the turbulent kinetic energy for three different conditions of nozzle-to-plate height. Barata et al. used laser-Doppler anemometry (LDA) to measure an impinging jet in a low-velocity cross flow. They reported distributions of the convection term and the production term in the budget equation for the turbulent kinetic energy. The study of Cooper et al. was unique in that they chose a fully-developed turbulent pipe flow as an inlet velocity condition for the purpose of providing experimental data suitable for the comparison with turbulence model calculation. They used a single-wire probe and a X-wire probe to

Address reprint requests to Dr. Koichi Nishino, Department of Mechanical Engineering and Materials Science, Yokohama National University, Tokiwadai 156, Hodogaya-ku, Yokohama 240, Japan.

Received 13 October 1995; accepted 10 February 1996

Int. J. Heat and Fluid Flow 17: 193–201, 1996

655 Avenue of the Americas, New York, NY 10010

0142-727X/96/$15.00
PII S0142-727X(96)00040-6

measure the axial and radial velocity components. The results obtained were referred to in the companion paper of Craft et al. for their assessment and improvement of the redistribution term in the stress equation model.

All the above-mentioned measurements, except for that of Barata et al. (1993), were based on the use of hot-wire anemometry. However, this anemometry may not be appropriate for the velocity measurement in the stagnation region of an impinging flow, especially near the impingement wall. This is because the flow in this region is highly turbulent, accompanied by unsteady flow reversals and separations, which may introduce large measurement errors when using the hot-wire technique. For this reason, particle-tracking velocimetry (PTV) was employed in the present study. Because PTV is able to resolve flow reversals and capture two or three velocity components simultaneously, it is suitable for the measurement of turbulent statistics in the stagnation region. Recently, Landreth and Adrian (1990) performed a velocity measurement of a circular impinging jet flow by using particle-image velocimetry (PIV). They demonstrated that the PIV technique was very suitable for accurate and resolved measurements of complex turbulent behavior in the stagnation region. Although they did not present detailed ensemble-averaged results, their study has encouraged the use of PIV/PTV for the measurement of impinging flows. The present measurements were done by using two-dimensional (2-D) and three-dimensional (3-D) PTVs, both developed by the authors. Some details of the PTV technique used here are described in the next section along with the flow facility and the present experimental conditions. The section on "Results and Discussion" describes the measured results of the mean velocities, the axial mean momentum balance, the Reynolds stresses, the turbulent kinetic energy, and the triple correlations of velocity fluctuations. The budget equation for the turbulent kinetic energy is also examined in that section, and some important aspects of turbulent transport mechanism are discussed. The main conclusions derived from the present study are summarized in the "Conclusion" section.

Method

Flow facility

All the measurements were made in a recirculating water tank facility. The water flow was driven by a centrifugal pump, whose rotational speed was precisely controlled by an inverter. A submerged circular nozzle 40 mm in inner diameter was placed on the bottom of the water tank (Figure 1). From the nozzle, a circular jet flow issued vertically upward and impinged on a flat glass plate held in the water. The distance between the nozzle and the plate was 234.4 mm, thus $H/D = 5.86$. This particular

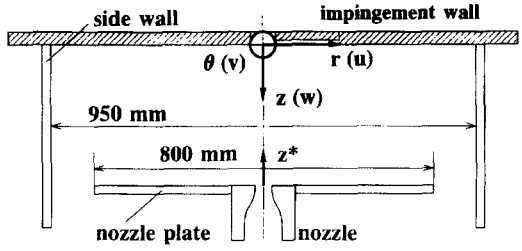

Figure 1 Measurement section and coordinate system

distance was selected by considering that the maximum heat and mass transfer at the stagnation point was known to occur at around this distance-to-diameter ratio. A circular nozzle plate 800 mm in diameter was installed flush with the mouth of the nozzle exit, and a radial flow passage between the nozzle plate and the impingement plate was formed. To achieve good flow axisymmetry, a cylindrical side wall made of a transparent plastic plate 5 mm thick was constructed. After impinging on the wall, the flow spread outward while forming a radial wall jet along the surface, and the flow finally went out of the measurement section through an annular gap between the nozzle plate and the side wall. The flow rate was monitored by means of the static pressure drop measured along a straight pipe section installed between the pump and the nozzle. Variations of the flow rate during the experiment were minimized to less than 2%. The water temperature was also kept constant within ± 0.5°C variations.

Experimental conditions are summarized in Table 1. In the 2-D PTV measurement, the axial flow velocity at the nozzle exit was 292.6 mm/s, giving the jet Reynolds number of 13,100. The nozzle exit velocity for the 3-D PTV measurement was slightly lower, resulting in the jet Reynolds number of 10,400. The origin of the coordinate system was taken at the stagnation point, as shown in Figure 1. Note that the z-direction is positive vertically downward, and $z^*(=H-z)$ is used to denote the opposite direction originating from the nozzle exit.

Table 1 Basic experimental conditions

		2-D PTV	3-D PTV
Nozzle diameter	D(mm):	40.0	40.0
Plate height	H(mm), H/D:	234.4, 5.86	225.3, 5.63
Nozzle exit velocity	W_0(mm/s):	292.6	233.0
Kinematic viscosity	ν(mm^2/s):	0.895	0.859
Reynolds number	Re$=DW_0/\nu$:	13100	10400

Notation

b_{ij}	turbulent stress anisotropy, $=\overline{u_iu_j}/\overline{u_ku_k}-\delta_{ij}/3$
b_w	half-width of W-profile
D	nozzle exit diameter
H	nozzle-to-plate height
k	turbulent kinetic energy
L	distance between the view point and the light sheet
P, p	Mean pressure and fluctuating pressure
Re	Reynolds number, $=W_0D/\nu$
r, θ, z	cylindrical coordinates
U, V, W	mean velocity components
u, v, w	velocity fluctuations
u_i	fluctuating velocity component in ith direction
W_c	mean centerline velocity
W_0	nozzle exit velocity
x_p, y_p	particle coordinates in the light sheet
z^*	axial coordinate, $=H-z$
II, III	second and third invariances of b_{ij}

Greek

Δt	time difference
ν	kinematic viscosity
$\overline{(\ )}$	mean value
$(\ )'$	turbulent intensity
$(\ )^*$	values corresponding to z^*

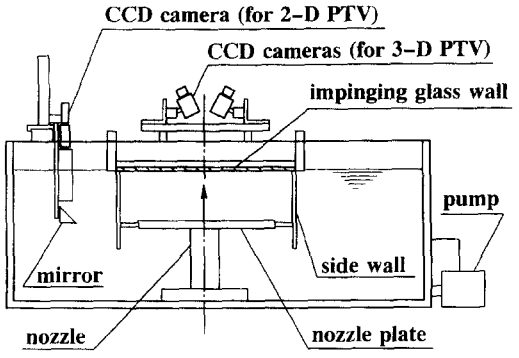

Figure 2 Camera arrangements for 2-D and 3-D PTVs

Particle-tracking velocimetry

The camera arrangements for 2-D PTV and 3-D PTV are illustrated in Figure 2. A 2-D PTV system developed by Adachi et al. (1993) was used to measure the axial and radial velocity components in a vertical plane of symmetry. A pulsed light sheet with half-width duration of 20 μs generated by a stroboscope was used for the illumination of that plane. The thickness and the width of the light sheet were approximately 5 mm and 100 mm, respectively. The light sheet was shed through the glass impingement plate to illuminate tracer particles suspended in the water. The tracer particles were made of nylon 12, whose average diameter and specific density were 150 μm and 1.02, respectively. Their motion was taken by a CCD camera by use of an inclined mirror so that the camera had a perpendicular view of the illuminated section. The size of a single viewing area was 88×92 mm^2, which was traversed horizontally and vertically in the plane of symmetry to measure the entire measurement cross section.

Television signals were digitized by an image grabber board which was interfaced with local parallel processors. For the 2-D PTV measurement, a set of consecutive 16 television fields taken at 60 Hz were digitized in real time. Approximately 200–300 tracer particles were recognized per television field. An efficient image-processing procedure was developed to calculate a centroid position of each particle image, and the data containing centroid positions were stored in the host computer for later analysis. These data acquisition procedures were repeated until sufficient data were accumulated so that reliable turbulence statistics could be evaluated. The data of centroid positions were later analyzed by a particle-tracking algorithm proposed by Nishino and Torii (1993). In this algorithm, velocity vectors were determined from the particle displacement during 1/30 s.

An example of instantaneous velocity vector distributions is shown in Figure 3. As shown here, velocity vectors obtained were located randomly in the viewing area. For taking an ensemble average at a fixed position in the flow field from those randomly located velocity vectors, a 2-D array of small rectangular cells was assigned so that the entire measurement cross section was divided into the array of cells. The size of the cell was set to be $\Delta r = 2$ mm and $\Delta z = 1$ mm in the stagnation region, and it was enlarged appropriately in the region where the flow characteristics would not vary significantly. A local ensemble average was taken from only those velocity vectors that were located inside the same cell. In the 2-D PTV measurement, the number of velocity vectors per cell exceeded 10,000 for most of the cells. A measurement uncertainty included in an instantaneous velocity vector was estimated to be 3.81 mm/s at a 95% confidence level for both axial and radial velocity components. The present data were evaluated to be valid near the wall up to $z = 1.5$ mm (or $z/D = 0.04$).

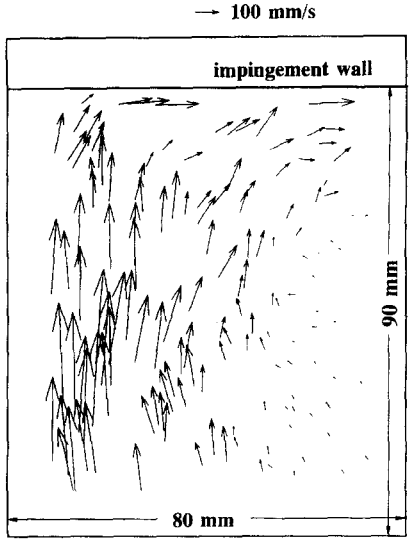

Figure 3 An example of instantaneous velocity vectors

A 3-D PTV system developed by Kato et al. (1992) was used for the simultaneous measurement of all three velocity components. Only the stagnation region was measured with a measuring volume of $100 \times 100 \times 72$ mm^3. The strobe light was shed parallel to the impingement plate, and observation with three CCD cameras was made through the impingement plate, as illustrated in Figure 2. Note that only two cameras are depicted in the figure. The tracer particles were the same as those used for 2-D PTV. The velocity was calculated from the particle displacement during 1/20 s. Uncertainty intervals associated with an instantaneous velocity vector were evaluated to be 1.8 mm/s for the radial and circumferential components and 13.8 mm/s for the axial component. This larger uncertainty in the axial component was caused by the particular camera arrangement taken presently; i.e., all the cameras were set above the impingement plate, thus viewing the jet flow from axially downstream positions. For taking ensemble averages of 3-D velocity vectors, the 2-D array of cells identical to that for 2-D PTV measurement was used after the circumferential averaging based on the flow axisymmetry was applied. The number of samples per cell were about 5000 or more, and the statistical results were evaluated to be valid near the wall up to $z = 4.5$ mm (or $z/D = 0.11$).

Here, it is worth mentioning the influence of the out-of-plane velocity on the present 2-D PTV measurement. As pointed out by one reviewer, a serious measurement error could be caused by the out-of-plane velocity if its magnitude is too large. As for this influence, there are two different factors to be considered; i.e., the velocity bias and the particle disappearance. The velocity bias, which was addressed in detail by Adrian (1991), is due to the spurious in-plane displacement caused by the out-of-plane displacement, as illustrated in Figure 4. The relative spurious in-plane displacement, $\Delta x/x_p$, is related to the geometrical parameters as $\Delta x/x_p = y_p/(L - y_p)$, where L represents the distance between the view point and the light sheet, and (x_p, y_p) represent the particle coordinates in the light sheet. In the present configuration, L is about 1000 mm, and y_p is at most 2.5 mm. Therefore, the relative spurious in-plane displacement does not exceed 0.25%. On the other hand, the influence of the particle disappearance can be examined by the comparison of possible out-of-plane displacements with the thickness of the light sheet. Because a plane of symmetry of the flow field is illuminated here, velocity fluctuations in the circumferential direction should be considered to evaluate out-of-plane displace-

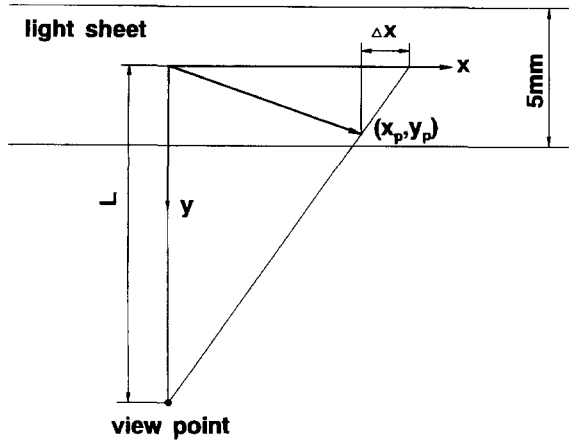

Figure 4 Spurious displacement due to out-of-plane velocity

ments. As shown later in Figure 12, the circumferential turbulent intensities in the stagnation region measured by the 3-D PTV are at most 12% of the nozzle exit velocity. Hence, the standard deviation of possible out-of-plane displacements becomes 1.2 mm ($= 0.12W_0\,\Delta t$, where $\Delta t = 1/30$ s), which is about a quarter of the thickness of the light sheet (5 mm). The above examinations, therefore, indicate that the out-of-plane velocity would not impose a serious influence on the present 2-D PTV measurement. This conclusion seems to be supported by the good agreement between 2-D PTV measurement and 3-D PTV measurement shown in Figures 10, 11, 14, and 15.

Results and discussion

Nozzle exit conditions and flow axisymmetry

Velocity conditions at the nozzle exit are given in Figure 5. These were obtained at 9.4 mm downstream of the nozzle exit. It is seen that the axial mean velocity is constant within the jet. The turbulent intensities in the axial and radial directions are measured respectively to be 3.8% and 8.3% of the nozzle exit velocity. Vortex stretching in the convergent nozzle should be the reason for this larger turbulent intensity in the radial direction than in the axial direction. Relatively high turbulence levels at the nozzle exit are the consequence of the absence of wire screens in the flow-settling section of the nozzle. The wire screens, which were originally designed to be installed in the nozzle, had to be removed in order to deal with particle sticking to the wires during measurement runs. The turbulent kinetic energy included in Figure 5 was evaluated from the assumption

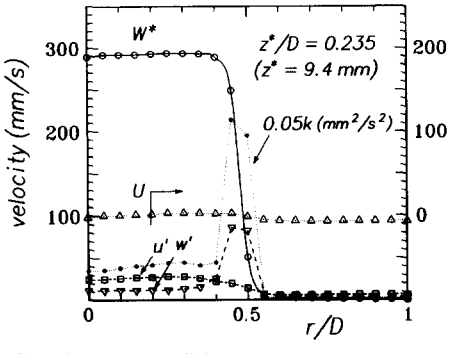

Figure 5 Nozzle exit conditions

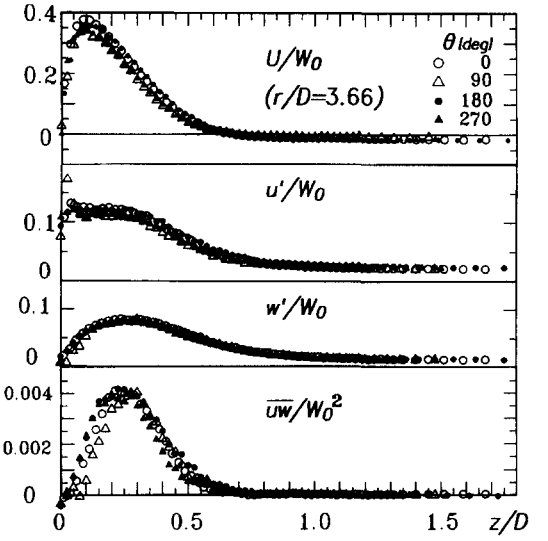

Figure 6 Flow axisymmetry shown by the mean velocity and the Reynolds stresses

that the circumferential turbulent intensity is equal to the radial one. This assumption should be reasonable for the turbulence caused by the vortex stretching in the convergent nozzle.

Flow axisymmetry was confirmed by the velocity measurements at four different circumferential locations ($\theta = 0°, 90°, 180°, 270°$) with constant radial distance ($r/D = 3.66$). As demonstrated in Figure 6, the radial mean velocity and the Reynolds normal and shear stresses agree well with each other, thus confirming a good flow axisymmetry. The absence of any swirling components in the stagnation region was also verified by the 3-D PTV measurement as shown later.

Mean momentum transport

Figure 7 shows the axial and radial mean velocity profiles in the stagnation region. As commonly done for the free jet, the axial component W is normalized by the local centerline velocity W_c, and the radial position r is normalized by the radial half width of W-profile b_w. It is found that the normalized W-profiles follow the Gaussian distribution even in the immediate vicinity of the

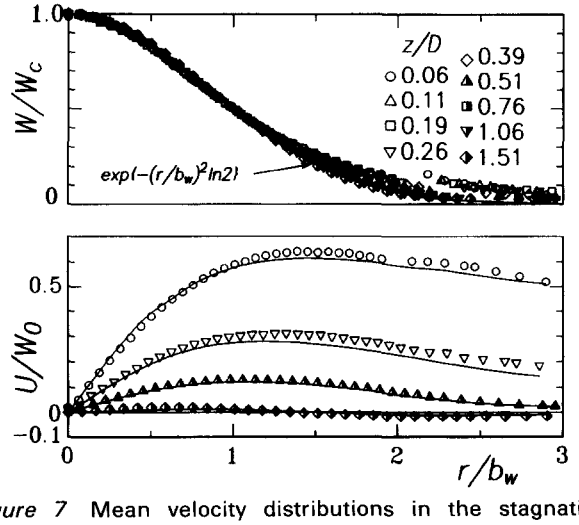

Figure 7 Mean velocity distributions in the stagnation region

wall (up to $z/D = 0.06$). This finding is in agreement with those reported previously by Ennohji and Asanuma (1982). The radial velocity U is normalized by the nozzle exit velocity. Its magnitude increases sharply as the wall is approached. To check the consistency of the present measurement for the mean velocities, the continuity equation is integrated by using the measured axial mean velocity distributions. The curves thus evaluated are compared with the measured radial mean velocity profiles in Figure 7. The curves are in satisfactory agreement with the measurement, hence supporting the consistency of the present measurement.

The axial mean momentum transport is expressed as follows:

$$U\frac{\partial W}{\partial r} + W\frac{\partial W}{\partial z} + \frac{\partial(\overline{ruw})}{r\,\partial r} + \frac{\partial \overline{w^2}}{\partial z} + \frac{\partial P}{\rho\,\partial z} = 0 \qquad (1)$$

where the viscous term is omitted, because it is found to be negligible here. Each term in Equation 1 was evaluated from the present data, where the pressure term was taken as residual. In Figure 8, the distribution of each term is plotted as a function of radial position along two horizontal lines, $z/D = 0.06$ and $z/D = 1.51$. The momentum balance at $z/D = 1.51$, the position relatively far from the impingement wall, is found to be similar to that of the free jet, in that the momentum transport near the jet axis is mostly undertaken by the axial convection ($W\,\partial W/\partial z$) and the turbulent shear stress ($\partial(\overline{ruw})/r\,\partial r$). Note that the position of the peak of these terms is slightly shifted from the jet axis, because the jet is still in a developing stage at this downstream location from the nozzle ($z^*/D = 4.35$). Very near the wall ($z/D = 0.06$), it is observed that the momentum transport is significantly enhanced. The axial convection ($W\,\partial W/\partial z$) and the turbulent normal stress ($\partial \overline{w^2}/\partial z$) are major source terms, and their momentum is converted to that of the static pressure. The contribution of the axial convection is simply due to the deceleration of the axial mean velocity toward the impingement wall. On the other hand, the contribution of the turbulent normal stress implies the occurrence of a substantial momentum transport from the turbulent field to the mean field very near the wall. As discussed in more detail later, this contribution of the turbulent normal stress is related to the net negative production of the turbulent kinetic energy near the impingement wall.

Centerline variations of the axial mean velocity, turbulent intensities, and others are presented in Figure 9. The mean velocity decays as the wall is approached; whereas, its half width increases gradually. The axial turbulent intensity w' first grows toward the wall with the development of the jet, then it starts to decrease sharply near the wall after taking a peak at $z/D = 0.25$.

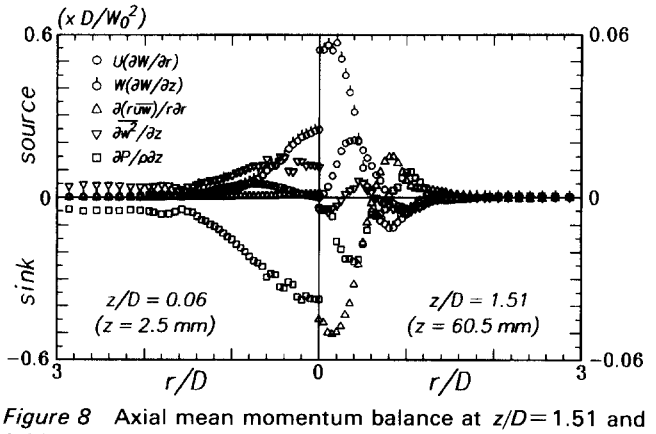

Figure 8 Axial mean momentum balance at $z/D = 1.51$ and 0.06

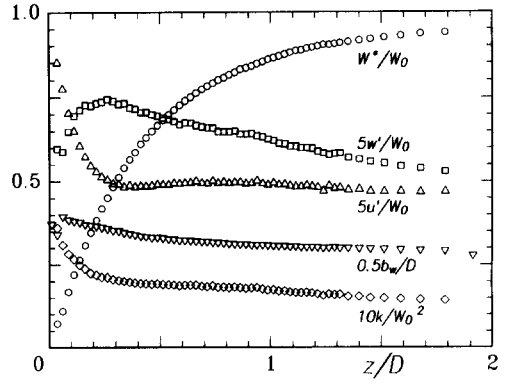

Figure 9 Variations of statistical quantities along the jet axis

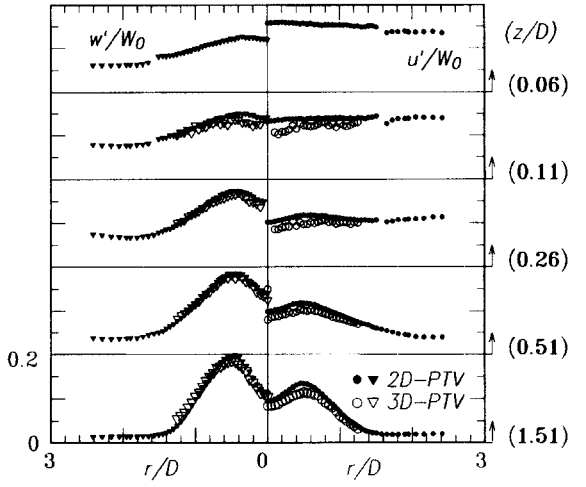

Figure 10 Turbulent intensities of axial and radial components

In contrast, the radial turbulent intensity u' shows a steep rise toward the wall, finally exceeding w' for $z/D < 0.1$. Because the magnitude of the circumferential turbulent intensity is equal to that of the radial component on the jet axis, the turbulent kinetic energy k exhibits an increase similar to that of the radial component near the wall.

Turbulence characteristics

Figure 10 shows the distributions of turbulent intensities u' and w'. The results obtained by 2-D PTV and 3-D PTV are in reasonable agreement. At $z/D = 1.51$, both turbulent intensities exhibit a sharp peak at around $r/D = 0.5$, reflecting the characteristics of the developing jet. This intense turbulence diffuses toward both the jet axis and the outer edge of the jet as the flow evolves downstream. Very near the wall ($z/D = 0.06$), w' is damped by the presence of the wall; whereas, u' is substantially enhanced. In consequence, u' becomes larger than w' for the entire radial extent shown here.

Turbulent shear stresses are presented in Figure 11. The values of $\overline{uv}$ and $\overline{vw}$ measured by 3-D PTV are all close to zero as required from the flow axisymmetry. As for the nonzero component $\overline{uw}$, the results obtained by 2-D PTV and 3-D PTV are again in fair agreement. The profiles of $\overline{uw}$ for $z/D > 0.26$ are mostly negative, showing a peak at around $r/D = 0.5$, while those for $z/D \leq 0.26$ are positive. This positive sign is consistent with the characteristics of the radial wall jet as recognized in Figure 6.

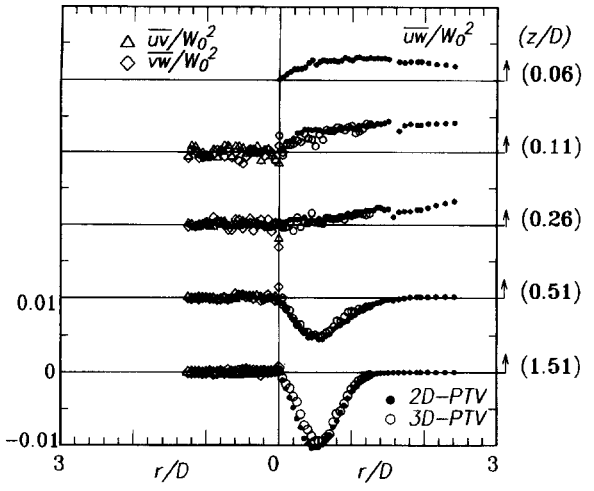

Figure 11 Turbulent shear stresses

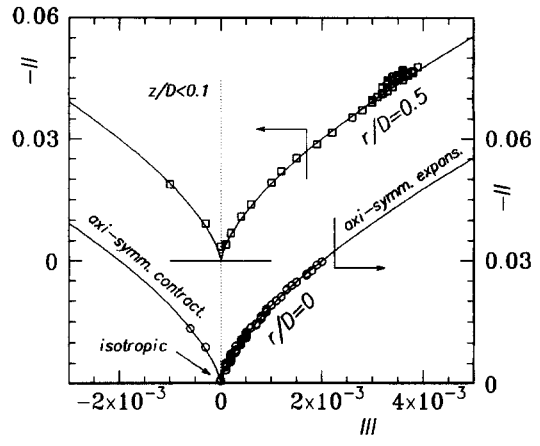

Figure 13 Anisotropy invariant map of the Reynolds stresses

Figure 12 compares the radial turbulent intensity with the circumferential turbulent intensity, both measured by the 3-D PTV. It is interesting to note that their distributions are almost identical; i.e.,

$$\overline{v^2}(r,z) \simeq \overline{u^2}(r,z) \tag{2}$$

This relationship suggests that the turbulence in the stagnation region is close to an axisymmetric state. Such a feature is better examined by the map of invariances of the turbulent stress anisotropy tensor b_{ij}. The invariances II and III are defined as follows:

$$-II = b_{ij}b_{ji}/2, \qquad III = b_{ij}b_{jk}b_{ki}/3 \tag{3}$$

The anisotropy invariant map is shown in Figure 13. Two vertical lines; i.e., $r/D = 0$ and $r/D = 0.5$, are chosen here along which variations of the invariances $(-II, III)$ are plotted for the range of $0.04 \le z/D \le 1.51$. For comparison, the curves corresponding to the axisymmetric expansion and the axisymmetric contraction are included. The first feature to be mentioned is that the values of III evaluated from the present data are very small, actually being limited in the range between -1×10^{-3} and 4×10^{-3}. This means that the turbulence is basically near to an isotropic state. The second feature to be mentioned is that the present data follow the axisymmetric expansion state for $z/D > 0.1$, while they follow the axisymmetric contraction state for $z/D < 0.1$. The former may be interpreted as a consequence of divergent streamlines in the stagnation region. On the other hand, the latter, which is a feature reflecting the fact of $u' > w'$ near the wall, is considered to be a unique consequence of the presence of the impingement wall.

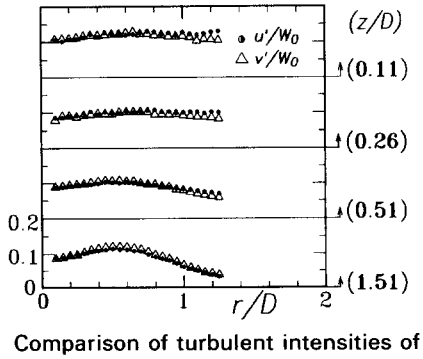

Figure 12 Comparison of turbulent intensities of the radial and circumferential components

Budget for turbulent kinetic energy

The budget equation for the turbulent kinetic energy is given as follows:

$$C_k + P_k + \varepsilon_k + TD_k + PD_k + VD_k = 0 \tag{4}$$

where:
convection:

$$C_k = -\frac{Dk}{Dt} = -U\frac{\partial k}{\partial r} - W\frac{\partial k}{\partial z}$$

production:

$$P_k = -\overline{u^2}\frac{\partial U}{\partial r} - \overline{uw}\frac{\partial U}{\partial z} - \overline{uw}\frac{\partial W}{\partial r} - \overline{w^2}\frac{\partial W}{\partial z} - \overline{v^2}\frac{U}{r}$$

dissipation:

$$\varepsilon_k = -\upsilon\overline{\frac{\partial u_i}{\partial x_j}\frac{\partial u_i}{\partial x_j}}$$

turbulent diffusion:

$$TD_k = -\left(\frac{\partial\overline{uk'}}{\partial r} + \frac{\overline{uk'}}{r} + \frac{\partial\overline{wk'}}{\partial z}\right)$$

pressure diffusion:

$$PD_k = -\frac{1}{\rho}\left(\frac{\partial\overline{pu}}{\partial r} + \frac{\overline{pu}}{r} + \frac{\partial\overline{pw}}{\partial z}\right)$$

viscous diffusion:

$$VD_k = \upsilon\left(\frac{\partial^2 k}{\partial r^2} + \frac{1}{r}\frac{\partial k}{\partial r} + \frac{\partial^2 k}{\partial z^2}\right)$$

The production term on the axis of symmetry can be simplified by using the axisymmetry conditions ($\overline{u^2} = \overline{v^2}$, $\partial U/\partial r = U/r$) and the continuity relation ($\partial W/\partial z = -\partial U/\partial r - U/r$) as follows:

$$P_k = 2(\overline{w^2} - \overline{u^2})(\partial U/\partial r) \tag{5}$$

The above expression means that the rate of production of the turbulent kinetic energy on the axis of symmetry is proportional to the difference of the turbulent normal stresses. Because the present data show $\partial U/\partial r > 0$ and $(\overline{w^2} - \overline{u^2}) < 0$ for $z/D < 0.1$, it is concluded that the net negative production of the turbulent kinetic energy takes place in this region. As pointed out earlier, this phenomenon is considered to be related to the net momentum transport from the turbulent field to the static pressure. It is, therefore, conjectured that the pressure field is playing an important roll for the turbulent energy transport near the impingement wall.

The triple correlations of velocity fluctuations are shown in Figure 14 as a function of r/D. As for $\overline{u^3}, \overline{uv^2}, \overline{uw^2}$ included in the first and second terms of TD_k, it is seen that $\overline{uw^2}$ is the leading term and that the profiles of $\overline{uv^2}$ are close to those of $\overline{u^3}$. Figure 15 presents the profiles of $\overline{u^2w}, \overline{v^2w}, \overline{w^3}$ as a function of z/D. These terms appear in the third term of TD_k. It is seen that $\overline{w^3}$ is the leading term and that $\overline{v^2w}$ is very close to $\overline{u^2w}$. From the similarity seen between $\overline{u^2v}$ and $\overline{u^3}$ and between $\overline{v^2w}$ and $\overline{u^2w}$, the following approximation may be justified for the evaluation of TD_k:

$$\overline{u_i v^2}(r,z) \simeq \overline{u_i u^2}(r,z) \qquad \text{for} \qquad i = 1,2,3 \tag{6}$$

where $\overline{v^3} = \overline{vu^2} = 0$ from flow axisymmetry. Equations 2 and 6 permit the examination of the k-budget by using only the 2-D PTV data, in which the circumferential velocity component v is not measured. As mentioned in the section "Method," the present measurement uncertainties associated with w-component are substantially larger in the 3-D PTV measurement than in the 2-D PTV measurement. In addition, the latter provide the data in the very vicinity of the wall ($0.04 \le z/D \le 0.11$). Therefore, the 2-D PTV data are used for the evaluation of the k-budget with the approximation of Equations 2 and 6 when necessary.

All the derivatives appearing in Equation 4 are evaluated by fitting the fourth-order B-spline functions to the experimental data. The radial and axial derivatives were obtained from the horizontal (constant z) data rows and the vertical (constant r) data rows, respectively. The fitted data are in the range of $0 \le r/D \le 4.9$ and $0.04 \le z/D \le 1.91$. The unmeasurable terms

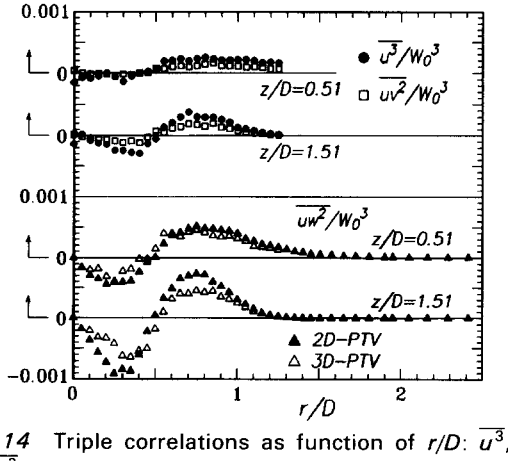

Figure 14 Triple correlations as function of r/D: $\overline{u^3}$, $\overline{uv^3}$, and $\overline{uw^2}$

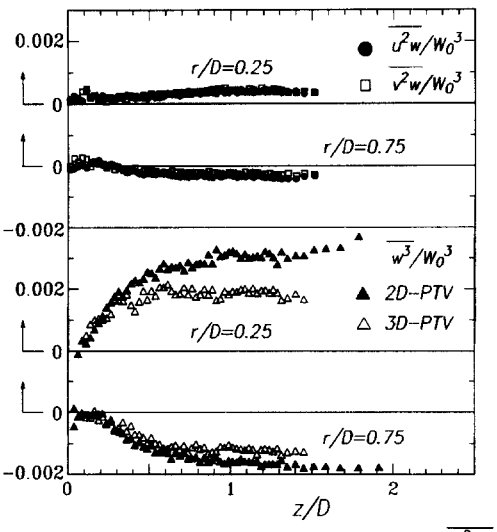

Figure 15 Triple correlations as function of z/D: $\overline{u^2w}$, $\overline{v^2w}$, and $\overline{w^3}$

in Equation 4, ε_k and PD_k, are estimated together as residual. The k-budget behaviors thus obtained along $r/D = 0$ and $r/D = 0.5$ are presented in Figure 16. Their characteristics may be summarized as follows.

Characteristics along r/D=0 (Figure 16a). First, in the region relatively far from the wall (say, $z/D = 1 \sim 1.5$), TD_k (mainly, $\partial\overline{uw^2}/\partial r$) represents a gain of turbulent kinetic energy; whereas, C_k and $(\varepsilon_k + PD_k)$ represent a loss. This is consistent with the well-known feature that TD_k is important in a developing stage of a jet. Second, the jet evolves downstream, TD_k

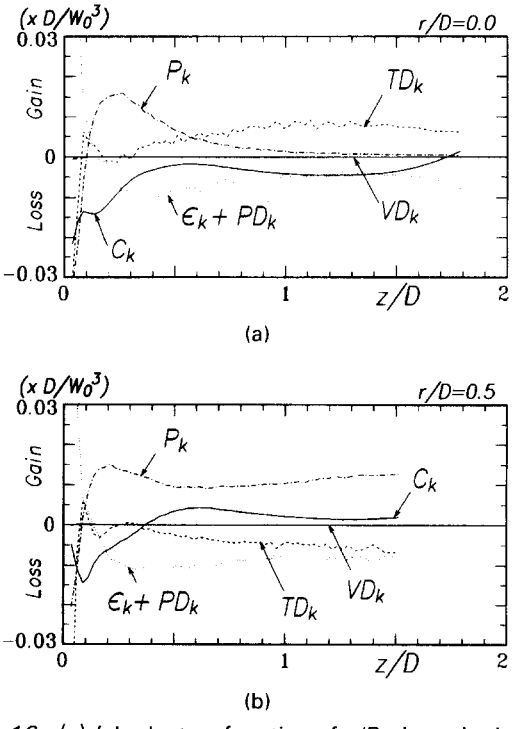

Figure 16 (a) k-budget as function of z/D along the jet axis; (b) k-budget as function of z/D along $r/D=0.5$

gradually decreases, while P_k starts to increase as a result of the development of the jet. Note that the rapid increase in P_k for $z/D < 0.5$ is due to the increase in both $\partial U/\partial r$ and $(\overline{w^2} - \overline{u^2})$. Third, very near the wall, P_k becomes negative after taking a positive peak at $z/D = 0.25$ and both C_k and TD_k (mainly, $\partial \overline{w^3}/\partial z$) also become negative, hence resulting in a large gain of the residual term. Because the dissipation must remain as a loss, the pressure diffusion should represent this large gain in the vicinity of the wall.

Characteristics along $r/D = 0.5$ (Figure 16b). Basically, the general trend of the budget is similar to that along $r/D = 0$, except that TD_k becomes a loss; whereas, P_k is a gain at around $z/D = 1 \sim 1.5$. This is due to the large production of turbulent kinetic energy by the turbulent shear stress $\overline{uw}$ at this radial location. The behavior near the wall is qualitatively similar to that along $r/D = 0$ in exhibiting a net negative production and a rapid increase in the residual term.

In Figure 17, profiles of the budget terms are plotted as a function of r/D along horizontal lines through $z/D = 1.51$ and $z/D = 0.06$. The production at $z/D = 1.51$ takes a maximum at around $r/D = 0.5$, the location corresponding to the jet shear layer. The turbulent kinetic energy produced here is transported by the turbulent diffusion toward the jet axis as well as toward the outer edge of the jet. Although no direct evidence was obtained, the pressure diffusion is conjectured to be responsible for the transport of the turbulent kinetic energy. All these features mentioned above are consistent with a widely believed picture of the turbulent transport mechanism in the developing jet. Such a mechanism is drastically changed near the impingement wall, as seen in Figure 17b. As already pointed out, only the pressure diffusion remains as a gain, and all other terms except for the viscous diffusion are acting as a loss of turbulent kinetic energy. This feature is observed for the radial position up to $r/D = 1.25$. Because this radial extent is corresponding to the area on which the remarkable heat and mass transfer augmentation will be achieved, the unique feature of turbulent transport mechanism revealed here should be related to the augmentation mechanism for heat and mass transfer on the stagnation area.

Finally, it is worth pointing out that the convection, production, turbulent diffusion, and pressure diffusion terms must vanish at the wall. Unfortunately, the present data could not cover such a near-wall region where the vanishing behavior would be observed. Further measurements with high spatial resolution are, therefore, needed to capture such near-wall behavior.

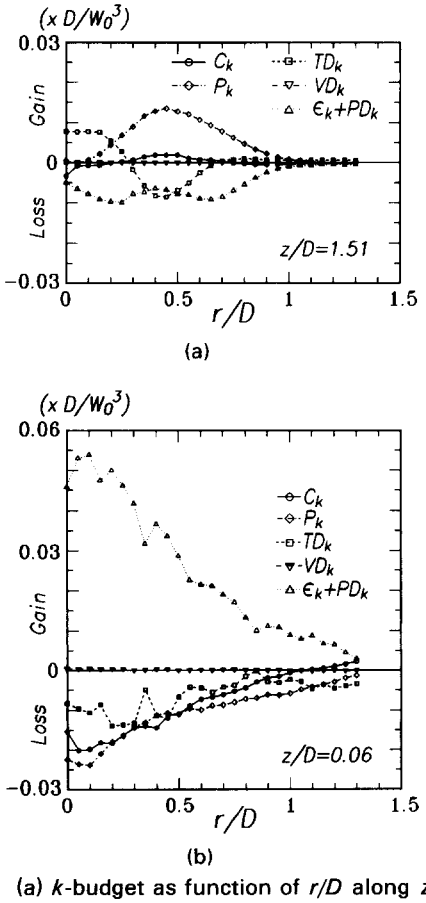

Figure 17 (a) k-budget as function of r/D along $z/D = 1.51$; (b) k-budget as function of r/D along $z/D = 0.06$

Conclusions

Turbulence statistics in the stagnation region of an axisymmetric impinging jet flow have been measured by using 2-D and 3-D particle-tracking velocimeters. Distributions of the mean velocities, the turbulent stresses and the triple correlations of velocity fluctuations were reported. Examination of the mean momentum balance indicated that the turbulent normal stress in the axial direction has a significant contribution to the increase in the static pressure near the wall. In this region, the axial turbulent intensity was reduced; whereas, the radial one was augmented. This resulted in the latter exceeding the former very close to the impingement wall. The state of turbulence was examined by the invariant map of the turbulent stress anisotropy. It was revealed that the turbulence in the stagnation region was close to an axisymmetric state. In addition, the present data showed that there were close similarities in turbulence statistics of the radial and circumferential velocity fluctuations. These similarities were utilized for the examination of the budget equation for the turbulent kinetic energy. It was shown that the negative production of the turbulent kinetic energy was taking place in the near-wall region where the excess of the radial turbulent intensity occurred. It was pointed out that the pressure diffusion term should compensate for the loss of turbulent kinetic energy caused by the negative production and other terms in this region.

Acknowledgments

The financial support through the Grant-in-Aid for Scientific Research on Priority Areas (Nos. 05240208 and 05240103) by the Ministry of Education, Science and Culture of Japan is acknowledged.

References

Adachi, T., Nishino, K. and Torii, K. 1993. Digital PTV measurements of a separated air flow behind a backward-facing step. *J. Flow Visualization and Image Processing*, **1**, 317–335

Adrian, R. J. 1991. Particle-imaging techniques for experimental fluid mechanics. *Ann. Rev. Fluid Mech.*, **23**, 261–304

Barata, J. M. M., Durão, D. F. G., Heitor, M. V. and McGuirk, J. J. 1993. On the analysis of an impinging jet on ground effects. *Exp. Fluids*, **15**, 117–129

Beltaos, S. and Rajaratnam, N. 1974. Impinging circular turbulent jets. *J. Hydraulics Division, Proc. American Society of Civil Engineers*, **100**, 1313–1328

Cooper, D., Jackson, D. C., Launder, B. E. and Liao, G. X. 1993. Impinging jet studies for turbulence model assessment—I. Flowfield experiments. *Int. J. Heat Mass Transfer*, **36**, 2675–2684

Craft, T. J., Graham, L. J. W. and Launder, B. E. 1993. Impinging jet studies for turbulence model assessment—II. An examination of the performance of four turbulence models. *Int. J. Heat Mass Transfer*, **36**, 2685–2697

Donaldson, C. D., Snedeker, R. S. and Margolis, D. P. 1971. A study of free jet impingement. Part 2. Free jet turbulent structure and impingement heat transfer. *J. Fluid Mech.*, **45**, 475–512

Ennohji, H. and Asanuma, T. 1982. Flow characteristics of the impingement region in an axisymmetric turbulent jet (normally impinging jet). *Proc. of the Faculty of Engineering of Tokai University*, **1**, 147–158, (in Japanese)

Era, Y. and Saima, A. 1975. An investigation of impinging jet (experiments by air, hot air and carbondioxide). *Trans. Japan. Soc. Mech. Engs.* **41**, 3259–3268, (in Japanese)

Gibson, M. M. and Launder, B. E. 1978. Ground effects on pressure fluctuations in the atmospheric boundary layer. *J. Fluid Mech.*, **86**, 491–511

Kato, M. and Launder, B. E. 1993. The modeling of turbulent flow around stationary and vibrating square cylinders. *Proc. 9th Symposium Turbulent Shear Flows*, Kyoto, Japan, 10.4.4–10.4.6

Kato, H., Nishino, K. and Torii, K. 1992. Application of a 3-D PTV to the measurement of turbulent air flows. *Flow Visualization VI*, Y. Tanida and H. Miyashiro, (eds.), Springer-Verlag, Berlin, 797–801

Landreth, C. C. and Adrian, R. J. 1990. Impingement of a low Reynolds number turbulent circular jet onto a flat plate at normal incidence. *Exp. Fluids* **9**, 74–84

Nishino, K. and Torii, K. 1993. A fluid-dynamically optimum particle tracking method for 2-D PTV: Triple pattern matching algorithm. In *Transport Phenomena in Thermal Engineering*, J. S. Lee, S. H. Chung and K. H. Kim, (eds.), Begel House, New York, 1411–1416

Sudou, K. and Hibara, H. 1991. Gas-jet impingement normal to a solid surface. *Trans. Japan. Soc. Mech. Engs.* **57(B)**, 3731–3737, (in Japanese)